



# AGO2 promotes tumor progression in KRAS-driven mouse models of non–small cell lung cancer

Jean Ching-Yi Tien<sup>a,b,1</sup>, Seema Chugh<sup>a,b,1</sup>, Andrew E. Goodrum<sup>a,b</sup>, Yunhui Cheng<sup>a,b</sup>, Rahul Mannan<sup>a,b</sup>, Yuping Zhang<sup>a,b</sup>, Lisha Wang<sup>a,b</sup>, Vijaya L. Dommeti<sup>a,b</sup>, Xiaoming Wang<sup>a,b</sup>, Alice Xu<sup>a,b</sup>, Jennifer Hon<sup>a</sup>, Carson Kenum<sup>a</sup>, Fengyun Su<sup>a,b</sup>, Rui Wang<sup>a,b</sup>, Xuhong Cao<sup>a,b,c</sup>, Sunita Shankar<sup>a,b</sup>, and Arul M. Chinnaiyan<sup>a,b,c,d,e,2</sup>

<sup>a</sup>Michigan Center for Translational Pathology, University of Michigan, Ann Arbor, MI 48109; <sup>b</sup>Department of Pathology, University of Michigan, Ann Arbor, MI 48109; <sup>c</sup>Howard Hughes Medical Institute, University of Michigan, Ann Arbor, MI 48109; <sup>d</sup>Department of Urology, University of Michigan, Ann Arbor, MI 48109; and <sup>e</sup>Rogel Cancer Center, University of Michigan, Ann Arbor, MI 48109

Contributed by Arul M. Chinnaiyan, March 30, 2021 (sent for review December 21, 2020; reviewed by Rafael Rosell and Phillip A. Sharp)

Lung cancer is the deadliest malignancy in the United States. Non–small cell lung cancer (NSCLC) accounts for 85% of cases and is frequently driven by activating mutations in the gene encoding the KRAS GTPase (e.g., *KRASG12D*). Our previous work demonstrated that Argonaute 2 (AGO2)—a component of the RNA-induced silencing complex (RISC)—physically interacts with RAS and promotes its downstream signaling. We therefore hypothesized that AGO2 could promote *KRASG12D*-dependent NSCLC in vivo. To test the hypothesis, we evaluated the impact of *Ago2* knockout in the *KPC (LSL-Kras<sup>G12D/+</sup>;p53<sup>fl/fl</sup>;Cre)* mouse model of NSCLC. In *KPC* mice, intratracheal delivery of adenoviral Cre drives lung-specific expression of a stop-floxed *KRASG12D* allele and biallelic ablation of *p53*. Simultaneous biallelic ablation of floxed *Ago2* inhibited *KPC* lung nodule growth while reducing proliferative index and improving pathological grade. We next applied the *KP<sup>HerfC</sup>* model, in which the Clara cell-specific *CCSP*-driven Cre activates *KRASG12D* and ablates a single *p53* allele. In these mice, *Ago2* ablation also reduced tumor size and grade. In both models, *Ago2* knockout inhibited ERK phosphorylation (pERK) in tumor cells, indicating impaired KRAS signaling. RNA sequencing (RNA-seq) of *KPC* nodules and nodule-derived organoids demonstrated impaired canonical KRAS signaling with *Ago2* ablation. Strikingly, accumulation of pERK in *KPC* organoids depended on physical interaction of AGO2 and KRAS. Taken together, our data demonstrate a pathogenic role for AGO2 in KRAS-dependent NSCLC. Given the prevalence of this malignancy and current difficulties in therapeutically targeting KRAS signaling, our work may have future translational relevance.

AGO2 | KRAS | nonsmall cell lung cancer

Lung cancer is the deadliest malignancy in the United States, causing more than a quarter of all annual cancer fatalities (1). Non–small cell lung cancer (NSCLC) accounts for 85% of lung cancer cases and is frequently driven by *KRAS* mutations (2). The *RAS* family, which also includes *HRAS* and *NRAS*, encodes small GTPases that transduce extracellular mitogenic signals by cycling between an active GTP-bound state and an inactive GDP-bound state. Intrinsic GTP hydrolysis is compromised in oncogenic *RAS* variants (3, 4). Resultant constitutive elevation of GTP-bound *RAS* promotes neoplastic transformation by hyperactivating downstream signaling pathways such as RAF-MEK-ERK (MAPK) and PI3 kinase (PI3K) (4–6). In NSCLC, activating *RAS* mutants encode oncogenic *KRASG12C*, *KRASG12V*, and *KRASG12D* (7). Efforts to design viable *KRAS* inhibitors have been ongoing for the last four decades, but hindered by key features of *RAS* structure and biochemistry. Structurally, *RAS* lacks adequate binding pockets for small molecule inhibitors. Biochemically, the active site binds GTP at picomolar affinity, hampering competitive inhibition (8, 9). Novel *KRASG12C* inhibitors have recently overcome these obstacles, showing clinical promise in treating solid tumors, including NSCLC (10, 11). Nonetheless, other oncogenic *KRAS* variants remain refractory. As such, recent work has aimed

to identify *KRAS*-interacting proteins that may be targeted to suppress its downstream signaling in tumor cells.

Our group employed immunoprecipitation and mass spectrometry to screen *KRAS*-interacting proteins. We identified Argonaute 2 (AGO2)—a key regulator of microRNA (miRNA)-induced gene silencing—as a direct *KRAS* binding partner. AGO2-*KRAS* interaction occurred in NIH 3T3 cells ectopically overexpressing wild-type (WT) *KRAS*, and in several cancer lines harboring mutant *KRAS* variants. In *KRASG12C*-expressing H358 NSCLC cells, AGO2 knockdown inhibited cell proliferation, blunted colony formation, and reduced phosphorylation of *RAS* signaling mediators AKT, mTOR, and RSP6. Together, these findings suggested AGO2 could promote *KRAS*-driven malignancies through up-regulation of *KRAS* signaling (12). Indeed, a follow-up study demonstrated that AGO2 enables tumor progression in a mouse model of pancreatic ductal adenocarcinoma (PDAC) harboring *KRASG12D* (13).

AGO2 is one of four members of the mammalian Argonaute (AGO) family (which also includes AGO1, AGO3, and AGO4) (14, 15). AGO proteins are essential components of the RNA-induced silencing complex (RISC). Within RISC, miRNAs loaded onto AGO engage in complementary binding with target mRNAs to repress

## Significance

**RAS proteins (HRAS, NRAS, and KRAS) integrate extracellular trophic signals to promote cell proliferation. Constitutively active KRAS drives tumor initiation and progression in nonsmall cell lung cancer (NSCLC). As RAS proteins are often refractory to direct pharmacological inhibition, RAS-interacting proteins are under investigation as potential drug targets. We previously found Argonaute 2 (AGO2) to bind RAS and positively regulate RAS-dependent signaling pathways. AGO2 knockdown blunted proliferation in NSCLC cells containing a KRAS-activating mutation. Here, we demonstrate that AGO2 promotes tumor progression in multiple mouse models of KRAS-driven NSCLC. In these animals, Ago2 knockout impairs tumor growth, lowers pathologic grade, and inhibits KRAS signaling. Targeting the AGO2-KRAS interaction may hold future therapeutic promise in NSCLC and other KRAS-driven malignancies.**

Author contributions: J.C.-Y.T., S.C., S.S., and A.M.C. designed research; J.C.-Y.T., S.C., A.E.G., Y.C., R.M., L.W., V.L.D., X.W., A.X., J.H., C.K., F.S., R.W., X.C., and S.S. performed research; J.C.-Y.T., S.C., R.M., Y.Z., S.S., and A.M.C. analyzed data; and J.C.-Y.T. and A.M.C. wrote the paper.

Reviewers: R.R., Quirón-Dexeu University Institute; and P.A.S., Massachusetts Institute of Technology.

The authors declare no competing interest.

This open access article is distributed under Creative Commons Attribution-NonCommercial-NoDerivatives License 4.0 (CC BY-NC-ND).

<sup>1</sup>J.C.-Y.T. and S.C. contributed equally to this work.

<sup>2</sup>To whom correspondence may be addressed. Email: arul@umich.edu.

This article contains supporting information online at <https://www.pnas.org/lookup/suppl/doi:10.1073/pnas.2026104118/-DCSupplemental>.

Published May 10, 2021.

their translation (16, 17). AGO2 is unique among its family members in that it has intrinsic endonuclease activity and therein directly catalyzes the degradation of mRNA species (18). Moreover, AGO2 functions in DICER-independent miRNA processing to facilitate conversion of specific pre-miRNAs to mature miRNAs (19, 20). AGO2 also promotes miRNA stability, as demonstrated by experiments showing reduced miRNA half-life after *AGO2* knockdown that can be restored with AGO2 reconstitution (21). Intriguingly, total miRNA levels are often lower in cancers than in the corresponding normal tissue (22). Moreover, reductions in specific miRNA species—including members of the *let-7* family in NSCLC—have been directly linked to tumorigenesis (23, 24). In contrast, AGO2 is up-regulated in multiple tumor types (25–29); and data from The Cancer Genome Atlas (TCGA) show *AGO2* gene amplification and increased *AGO2* expression to be common in NSCLC (30). The discordance between expression patterns of miRNAs and *AGO2* in clinical cancer samples suggests that AGO2 might promote tumorigenesis through miRNA-independent mechanisms, such as regulation of KRAS signaling (12). To date, however, loss-of-function studies examining the *in vivo* role of AGO2 in NSCLC have not been performed. Here, we employ multiple genetically engineered mouse models to test the hypothesis that AGO2 promotes KRAS signaling and drives tumorigenesis in NSCLC.

## Results

**Genetic Ablation of *Ago2* Impairs Tumor Growth in Lung Adenocarcinoma Driven by *KrasG12D* Expression and *p53* Loss.** In order to define the contribution of *Ago2* to NSCLC, we analyzed the impact of its genetic ablation in the established *KPC* mouse model. *KPC* animals harbor both a stop-floxed *KrasG12D* transgene and two floxed *p53* alleles. When subjected to intratracheal delivery of Cre recombinase-expressing adenovirus (Adeno-Cre) they develop tumors consistent with NSCLC (31, 32). By intercrossing *KPC* animals and mice harboring floxed *Ago2* alleles (33), we generated progeny with concurrent homozygous (*KPC-Ago2<sup>-/-</sup>*) or heterozygous (*KPC-Ago2<sup>+/-</sup>*) ablation of *Ago2*. Sixteen weeks after administration of Adeno-Cre we analyzed tumor burden in these groups versus control *KPC* animals with wild-type *Ago2* expression (*KPC-Ago2<sup>+/+</sup>*) (SI Appendix, Fig. S1A). Immunohistochemistry demonstrated robust *Ago2* expression across the lung parenchyma and within tumor lesions of *KPC-Ago2<sup>+/+</sup>* mice. Over 90% of lesions from lungs of *KPC-Ago2<sup>-/-</sup>* animals showed no detectable AGO2 staining, indicating good knockout efficiency (SI Appendix, Fig. S1 B and C).

As previously reported (31) *KPC-Ago2<sup>+/+</sup>* animals developed significant tumor burden at the 16-wk time point, with numerous nodules visible on gross inspection of the lungs (Fig. 1A). While the number of grossly visible nodules was unchanged in the *KPC-Ago2<sup>+/-</sup>* group, it was significantly lower in *KPC-Ago2<sup>-/-</sup>* mice versus *KPC-Ago2<sup>+/+</sup>* controls (Fig. 1 A and B). Analysis of histological cross-sections, in which tumor inclusions are appreciable as hematoxylin-rich densities, showed that while nodule number per unit of cross-sectional area was unchanged among groups, average nodule size was markedly lower in *KPC-Ago<sup>-/-</sup>* animals versus both *KPC-Ago2<sup>+/+</sup>* and *KPC-Ago2<sup>+/-</sup>* mice (Fig. 1 C–E). As such, the reduction in total lung area occupied by tumor tissue seen with homozygous *Ago2* ablation (Fig. 1F) was driven by reduction in nodule size, rather than nodule number. Together, these findings indicate that AGO2 promotes NSCLC tumor growth.

**AGO2 Facilitates Progression of *KPC* Lung Adenocarcinoma.** Adenocarcinoma comprises much of the lung tumor burden in the *KPC* model (31). In keeping with these findings, we observed advanced (grades 3 and 4) adenocarcinoma lesions (SI Appendix, Fig. S2A) within lungs of *KPC* mice 16 wk after Cre administration. Indeed, in *KPC-Ago2<sup>+/+</sup>* and *KPC-Ago2<sup>+/-</sup>* mice, adenocarcinoma

occupied >10% of total lung cross-sectional area (Fig. 2A). In contrast, adenocarcinoma occupied <3% of cross-sectional area in *KPC-Ago2<sup>-/-</sup>* animals (Fig. 2A). Furthermore, grade 4 adenocarcinoma comprised >75% of tumor lesion cross-sectional in *KPC-Ago2<sup>+/+</sup>* and *KPC-Ago2<sup>+/-</sup>* mice, but only 25% in *KPC-Ago2<sup>-/-</sup>* mice (Fig. 2A). Consistent with this, while grade 4 lesions, were uniformly observable in both *KPC-Ago2<sup>+/+</sup>* and *KPC-Ago2<sup>+/-</sup>* animals, nearly half of *KPC-Ago2<sup>-/-</sup>* mice were completely free of tumors reaching that pathologic grade (Fig. 2B). Notably, in *KPC-Ago2<sup>-/-</sup>* mice, the infrequently observed AGO2(+) tumor nodules (SI Appendix, Fig. S1C) actually comprised the majority of grades 3 and 4 disease (SI Appendix, Fig. S2B). Indeed, AGO2(+) nodules within *KPC-Ago2<sup>-/-</sup>* lungs had similar adenocarcinoma frequency to those in *KPC-Ago2<sup>+/+</sup>* mice (SI Appendix, Fig. S2 B and C).

*KPC-Ago2<sup>-/-</sup>* mice were also partially protected from the overt bronchial invasion seen in the vast majority of *KPC-Ago2<sup>+/+</sup>* and *KPC-Ago2<sup>+/-</sup>* animals (Fig. 2B). Tumor proliferation index, assessed by Ki67 staining, was also significantly reduced with genetic *Ago2* ablation (Fig. 2 C and D). Finally, the reduced rate of tumor progression observed in the *KPC-Ago2<sup>-/-</sup>* group corresponded with increased survival versus animals of other genotypes (SI Appendix, Fig. S3).

***Ago2* Ablation Also Lowers Tumor Burden in Clara Cell-Derived, *KrasG12D*-Dependent Lung Cancer.** We next interrogated AGO2 function in two additional NSCLC models by employing animals that contain a tamoxifen (Tam)-inducible Cre recombinase gene driven by the (Clara cell-specific) CCSP (CC10) promoter (34). In the first model, we intercrossed Tam-inducible *CCSP-Cre* animals with stop-floxed *KrasG12D* mice to enable time-dependent activation of *Kras* oncogene. This is commonly referred to as the KC model (SI Appendix, Fig. S4A). As previously reported, KC mice develop epithelial hyperplasia by 3 wk, adenoma by 6 wk, and occasional adenocarcinoma 15 wk after Cre activation. The lungs of these animals also contain a macrophage-predominant inflammatory infiltrate (35). By intercrossing *Ago2* floxed animals into the KC line, we generated *KCAgo2<sup>+/+</sup>*, *KCAgo2<sup>+/-</sup>*, and *KCAgo2<sup>-/-</sup>* mice and treated with Tam (50 mg/kg, delivered by intraperitoneal injection) at 6 wk of age to initiate tumor formation (SI Appendix, Fig. S4B). Sixteen weeks later, we killed the animals and noted lung nodules in *KCAgo2<sup>+/+</sup>* mice, as previously described (35) (SI Appendix, Fig. S4C). Pathologic subtypes ranged from hyperplasia to frank adenocarcinoma, while inflammation was broadly appreciable in lungs of most animals (SI Appendix, Fig. S4D). Though the frequencies of hyperplasia and adenoma were largely unchanged with *Ago2* ablation, adenocarcinoma was absent in all *KCAgo2<sup>-/-</sup>* mice analyzed (SI Appendix, Fig. S4D). Unfortunately, the prominent lung inflammation inherent in this model complicated analysis of AGO2 function, as several mice in all groups died prematurely from pulmonary edema.

To circumvent the interference of inflammation with tumor analysis, we generated a more aggressive NSCLC model by employing the inducible CCSP Cre to simultaneously ablate one *p53* allele while activating *KrasG12D* transcription. These mice, here called *KP<sup>Het</sup>C*, also sequentially develop alveolar adenoma and adenocarcinoma (36). We interbred *KP<sup>Het</sup>C* animals with mice harboring floxed *Ago2* alleles to obtain *KP<sup>Het</sup>C-Ago2<sup>+/+</sup>*, *KP<sup>Het</sup>C-Ago2<sup>+/-</sup>*, and *KP<sup>Het</sup>C-Ago2<sup>-/-</sup>* progeny (SI Appendix, Fig. S5A). In each group, we induced Cre activation with Tam at 6 wk old, then evaluated tumor burden 18 wk later. Upon necropsy, gross nodules were visible in more than 75% of *KP<sup>Het</sup>C-Ago2<sup>+/+</sup>* and *KP<sup>Het</sup>C-Ago2<sup>+/-</sup>* mice. On the contrary, only 6 of 19 *KP<sup>Het</sup>C-Ago2<sup>-/-</sup>* mice had evidence of these tumors (Fig. 3A). Average number of gross nodules per animal was also lower in *KP<sup>Het</sup>C-Ago2<sup>-/-</sup>* mice versus the other groups (Fig. 3B). In histological cross-sections, the size of individual adenocarcinoma lesions was lower in a *KP<sup>Het</sup>C-Ago2<sup>-/-</sup>* versus the other genotypes, while total area occupied by adenocarcinoma was lower in *KP<sup>Het</sup>C-Ago2<sup>-/-</sup>* than

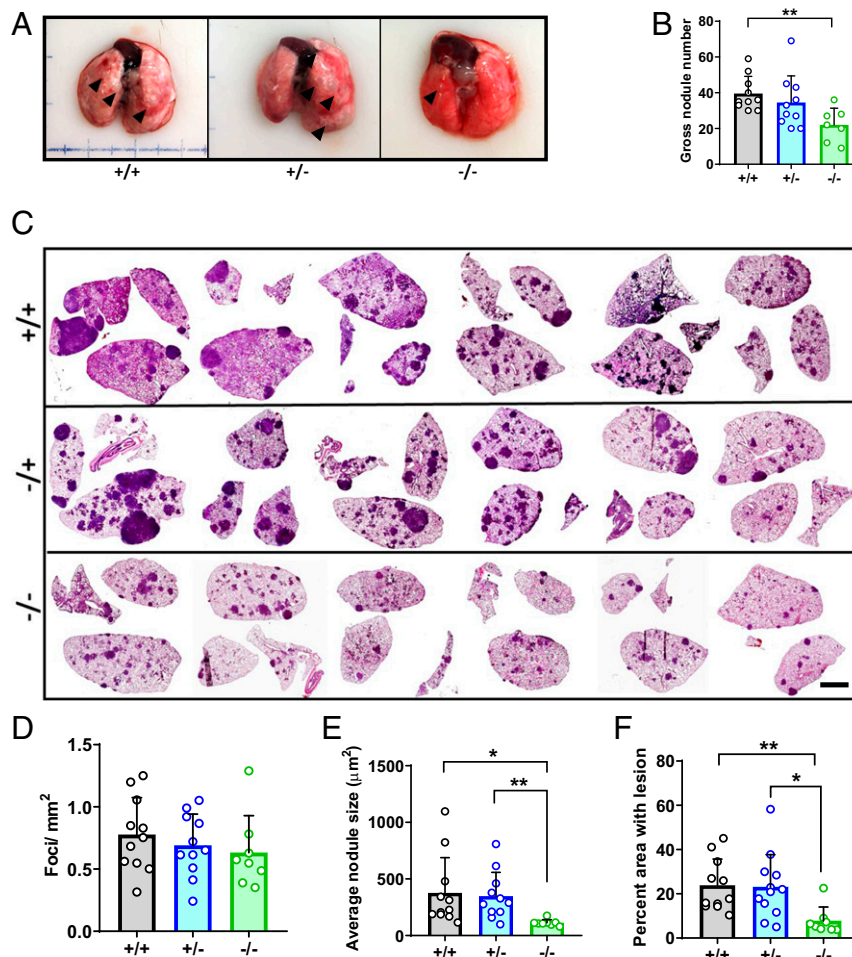


**Fig. 1.** *Ago2* ablation impairs tumor growth in KPC lung cancer. (A) Gross lung samples from *KPC-Ago2*<sup>+/+</sup> (+/+), *KPC-Ago2*<sup>+/-</sup> (+/-), and *KPC-Ago2*<sup>-/-</sup> (-/-) mice. Representative images from *n* = 11, *n* = 11, and *n* = 8 animals per group, respectively. Arrowheads indicate grossly visible tumor nodules. (B) Quantification of grossly visible nodules from aforementioned animals expressed as number of total nodules per pair of lungs. (C) Representative H&E-stained image series of lung cross-sections from +/+, +/-, and -/- mice. (Scale bar, 2.5 mm.) (D) Quantification of tumor foci per mm<sup>2</sup> cross-sectional area. Average of three non-consecutive sections from each of 11 +/+, 11 +/-, and 8 -/- animals. (E) Average surface area of individual nodules described in D. (F) Percentage of total lung cross-sectional area occupied by tumor lesion in the same animals as described in C–E. \**P* < 0.05, \*\**P* < 0.01.

*KP*<sup>Het</sup>*Cago2*<sup>+/+</sup> mice (Fig. 3 C–E and *SI Appendix, Fig. S5B*). We further observed that adenocarcinoma lesions in lungs of *KP*<sup>Het</sup>*Cago2*<sup>+/+</sup> mice were uniformly grade 4. Less advanced grade 3 lesions were more common with loss of 1 or both copies of *Ago2* (Fig. 3F). Reduction in tumor nodule size and pathologic grade corresponded with lower cell proliferation (as indicated by Ki67 index) in *KP*<sup>Het</sup>*Cago2*<sup>-/-</sup> mice (Fig. 3G). Taken together, these data demonstrate that AGO2 is required for the growth and progression of Clara cell-derived NSCLC.

***Ago2* Ablation Suppresses KRAS Signaling in NSCLC.** Since our previous work identified AGO2 as a positive regulator of canonical KRAS signaling (12), we performed immunohistochemistry for phosphorylated ERK (pERK) and noted reduced staining in lung nodules of *KPC-Ago2*<sup>-/-</sup> versus *KPC-Ago2*<sup>+/+</sup> mice (Fig. 4A). Immunoblot similarly demonstrated lower pERK levels in the setting of *Ago2* ablation (Fig. 4B). In contrast, immunoblots for phosphorylated AKT (pAKT) were similar between groups (Fig. 4B). Moreover, immunohistochemistry showed pAKT staining to be intense in ductal cells, but only scanty positive in tumor nodules, with no obvious intergroup differences (*SI Appendix, Fig. S6A*). To determine whether *Ago2* ablation reduced KRAS-dependent gene expression in the same lesions, we subjected nodule isolates to RNA sequencing

(RNA-seq), then performed gene set enrichment analysis (GSEA) employing signatures defined in KRAS-driven mouse lung cancer (37). Our analysis revealed KRAS-induced genes to be down-regulated and KRAS-repressed genes to be up-regulated in *KPC-Ago2*<sup>-/-</sup> versus *KPC-Ago2*<sup>+/+</sup> animals (Fig. 4C). Together, these data indicate AGO2 positively regulates MAPK signaling in *KPC* lung cancer. Tumor nodules from *KP*<sup>Het</sup>*C* mice were too small to be individually isolated; however, analysis of pERK distribution by immunohistochemistry also revealed reduced staining in *KP*<sup>Het</sup>*Cago2*<sup>-/-</sup> versus *KP*<sup>Het</sup>*Cago2*<sup>+/+</sup> nodules (Fig. 4D).

We then applied high-throughput QPCR to assess levels of 239 miRNAs in tumor nodule samples isolated from *KPC-Ago2*<sup>+/+</sup> and *KPC-Ago2*<sup>-/-</sup> mice. We found 11 species to be differentially expressed between groups (Fig. 4E). Among those up-regulated with *Ago2* ablation was *let-7c* (Fig. 4E). This and other members of the *let-7* family collectively decline in KRAS-driven NSCLC, promoting tumorigenesis (23, 24). Notably, MAPK signaling itself reduces *let-7* levels by stimulating LIN28, an inhibitor of *let-7* maturation (24). As such, impact on miRNA dynamics—either direct, or via canonical KRAS signaling—represents an interrelated mechanism by which AGO2 induces NSCLC progression in the *KPC* model. *miR-214*—a species for which both oncogenic and



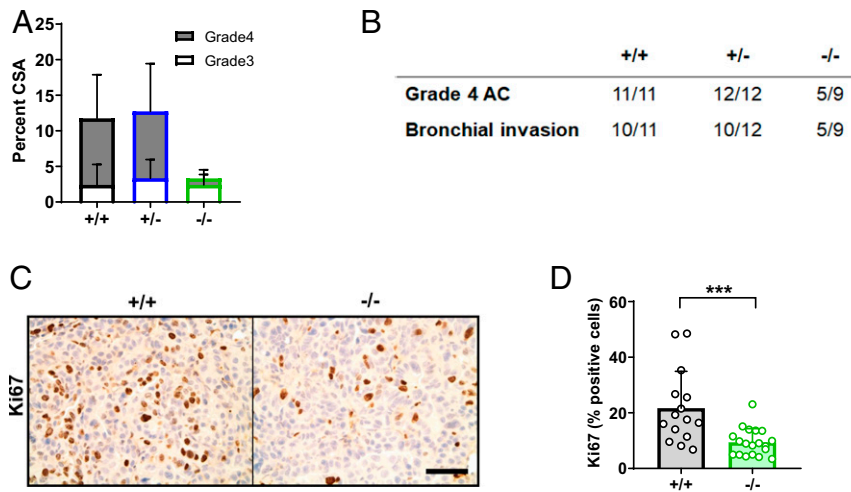


**Fig. 2.** Ago2 facilitates progression of KPC lung adenocarcinoma. (A) Percentage of lung cross-sectional area occupied by adenocarcinoma (subdivided into grade 3 and grade 4) in *KPC-Ago2*<sup>+/+</sup> (*+/+*) (*n* = 11), *KPC-Ago2*<sup>+/-</sup> (*+/-*) (*n* = 12), and *KPC-Ago2*<sup>-/-</sup> (*-/-*) (*n* = 9) mice. Analyses based on pathological assessment of H&E staining of whole lung cross-sections. (B) Number of mice per group (represented as a fraction of total animals) with any evidence of grade 4 adenocarcinoma (AC) or bronchial invasion. (C and D) Ki67 staining in adenocarcinoma lesions from *+/+* and *-/-* animals with quantification (*n* = 3 sections/animal, 6 animals/group). (Scale bar, 50  $\mu$ m.) \*\*\**P* < 0.001.

tumor suppressor roles have been reported in lung NSCLC (38–40)—was also elevated in *KPC-Ago2*<sup>-/-</sup> samples.

To further dissect the mechanistic link between AGO2 and canonical KRAS signaling in this system, we dissociated *KPC* tumor nodules and cultured cells ex vivo as organoids (41, 42). Consistent with our in vivo findings, organoids derived from *KPC-Ago2*<sup>-/-</sup> nodules were smaller (Fig. 5A and B) and had lower proliferation indices (Fig. 5B) than *KPC-Ago2*<sup>+/+</sup> organoids. RNA-seq with GSEA recapitulated findings from fresh nodule isolates, showing *Ago2* ablation to confer significant reduction in KRAS-induced genes and increase in KRAS-repressed genes (Fig. 5C). We previously defined direct protein–protein interaction as required for AGO2 regulation of KRAS signaling (12). In cells derived from organoids and grown in 2D culture, immunoprecipitation confirmed AGO2-RAS binding (*SI Appendix*, Fig. S6B). Organoid-derived cells lacking *Ago2* had lower proliferative rates (*SI Appendix*, Fig. S6C and D) and pERK levels (Fig. 5D) than those with intact *Ago2*. In order to determine whether direct interaction with KRAS was required for MAPK signaling in these cells, we transfected *KPC-Ago2*<sup>-/-</sup> cells with constructs encoding 1) wild-type AGO2, 2) AGO2K112A/E114A [deficient KRAS binding (12)], and 3) AGO2K98A [able to bind to KRAS (12)]. While add-back of WT AGO2 and AGO2K98A both induced higher pERK levels, addition of AGO2K112A/E114A did not (Fig. 5D). These findings demonstrate that in *KPC* tumor cells AGO2 promotes canonical MAPK signaling through direct interaction with AGO2.

## Discussion

In Western countries, activating *KRAS* mutations underlie 30% of NSCLC and predict negative outcomes in early- and late-stage disease (43). The clinical relevance of aberrant RAS signaling in this and other cancer types has prompted a long-standing search for effective RAS inhibitors that has been hampered by structural and biochemical features of the RAS molecule (8, 9). Attempts to block downstream effectors, disrupt RAS subcellular localization, and identify synthetic lethal partners have also met with only limited clinical success (44). In this setting, the search for KRAS interaction partners represents an alternate approach for identifying new drug targets. We recently defined AGO2 as a binding partner of both native KRAS and its mutant variants.

Interaction with AGO2 promotes KRAS downstream signaling, and *AGO2* knockdown inhibits proliferation and colony formation in *KRASG12C*-expressing H358 NSCLC cells (12). In the current study, we establish AGO2 as an in vivo mediator of NSCLC progression and positive regulator of MAPK signaling through direct KRAS binding.

*KRAS* mutant tumors are relatively unique among oncogene-driven NSCLCs in that they often harbor additional genetic alterations, including mutations in *STK11*, *CDKN2A/B*, and *p53* (45). Genetically engineered NSCLC mouse models recapitulate this aspect of human disease through conditional expression of one *KrasG12D* allele and ablation of one or both *p53* alleles (32). In *KPC* mice, intratracheal Adeno-Cre administration yields *KrasG12D* expression and biallelic *p53* knockout predominantly in alveolar type II cells (with lesser contribution from Clara cells). Early hyperplastic and adenomatous lesions precede the development of frank adenocarcinoma (46). Biallelic *Ago2* ablation in *KPC* mice yielded smaller tumor nodules with reduced proliferative index and pathologic grade. In the *KP<sup>HetC</sup>* model, the Clara cell-specific CCSP Cre drives expression of *KrasG12D* allele and knockout of a single *p53* allele. Our observation of inhibited tumor progression, reduced proliferative index, and down-regulated MAPK signaling in *KP<sup>HetC</sup>Ago2*<sup>-/-</sup> mice demonstrates that the effects of *Ago2* ablation are consistent across mouse NSCLC models with different primary cells of origin and *p53* loss status.

In both *KPC* and *KP<sup>HetC</sup>* models, inhibition of tumor progression corresponded with lower pERK levels in tumor nodules and/or nodule-derived organoids. Conversely, PI3K signaling was not obviously impacted. Our findings parallel those of several groups who demonstrated amplification of canonical MAPK signaling corresponds with progression of *KRASG12D*-driven murine adenocarcinoma (47–49). Clinical data demonstrating partial efficacy of the Mek1/2 inhibitor selumetinib in prolonging progression-free survival in *KRAS*-mutant NSCLC suggests a direct causative role for MAPK signaling in progression of analogous human tumors (50). Furthermore, Cicchini et al. directly tested this premise through forced amplification of MAPK signaling in nascent and established murine lung adenocarcinoma. In *KRASG12D*-expressing tumors derived from both alveolar type 2 cells and Clara cells, MAPK signaling was necessary for progression—particularly in *p53*-mutant disease (51). As such, our observation of reduced pERK in *Ago2*<sup>-/-</sup>

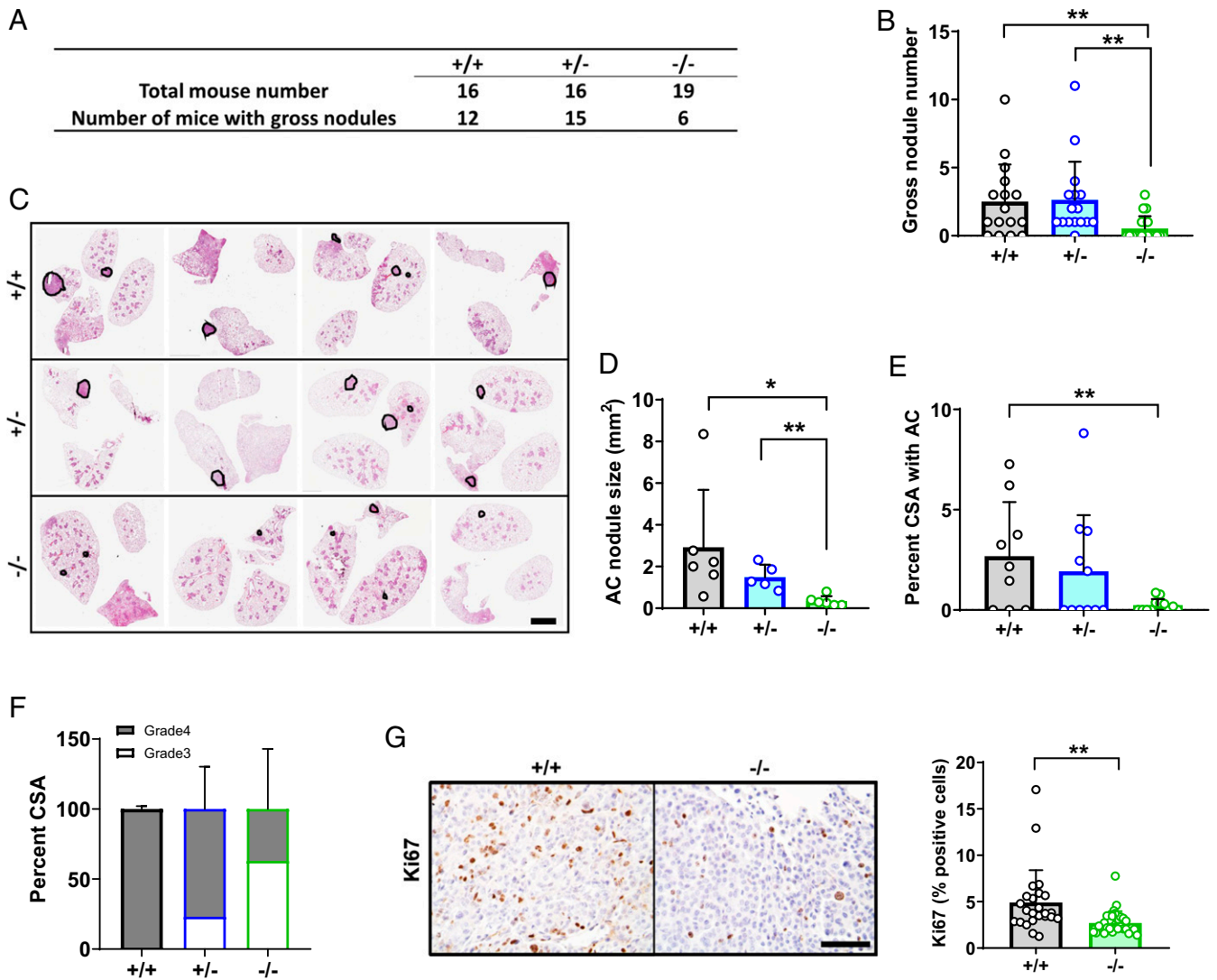


**FIG. 3.** *Ago2* ablation impairs tumor growth in *KP<sup>Het-C</sup>* lung cancer. (A and B) Quantification of grossly visible nodules from lungs of *KP<sup>Het-C</sup>-Ago2<sup>+/+</sup>* (+/+), *KP<sup>Het-C</sup>-Ago2<sup>+/-</sup>* (+/-), and *KP<sup>Het-C</sup>-Ago2<sup>-/-</sup>* (-/-) mice. (C) Representative H&E-stained image series of lung cross-sections from +/+, +/-, and -/- mice. (Scale bar, 2.5 mm.) (D) Quantification of adenocarcinoma (AC) foci per mm<sup>2</sup> cross-sectional area. (E) Average lung cross-sectional surface area (CSA) occupied by adenocarcinoma. (F) Percent grade 3 and grade 4 tissue within adenocarcinoma lesions of mice of each genotype. (G) Ki67 staining (Left images) and proliferative index (Right) in +/+ and -/- mice. (Scale bar, 50  $\mu$ m.) *n* = 16 to 19 mice/group. \**P* < 0.05, \*\**P* < 0.01.

*KPC* and *KP<sup>Het-C</sup>* mice strongly suggests *Ago2* ablation limits tumor progression by down-regulating MAPK signaling. The coincident increase of *let-7c-5p* observed in *KPC-Ago2<sup>-/-</sup>* versus *KPC-Ago2<sup>+/+</sup>* nodules may also occur downstream of MAPK signaling and represents a parallel mechanism by which *Ago2* loss impairs tumor progression in this model.

While our findings can be well integrated into the existing literature on *KRASG12D*-driven mouse models of lung cancer, comparison with other cell types in which AGO2 is genetically manipulated or inhibited reveals interesting differences that suggest context-specific consequences of *KRAS*-AGO2 interaction. For instance, in *KRASG12C*-expressing H358 cells AGO2 principally promotes RAS signaling through the PI3K pathway, as AGO2 knockdown causes a reduction in pAKT (12). In contrast, the KC mouse model of PDAC—in which the *p48* Cre drives *KrasG12D* expression in the exocrine pancreas—undergoes bona fide oncogene-induced senescence upon genetic *Ago2* ablation—blocking progression of early lesions to advanced adenocarcinoma (13). Interestingly, in that model, *Ago2* ablation had no effect on PDAC progression in the setting of *p53* loss (13). Taken together,

these findings suggest AGO2 inhibition might be applied to target multiple forms of *KRAS*-driven cancer with different downstream effector pathways (44). Based on this potential pharmacologic flexibility, the AGO2-*KRAS* interaction warrants further study in NSCLC and other *KRAS*-driven malignancies.

**Methods**

**Animals.** Mice of the following strains were obtained from The Jackson Laboratory: *Ago2<sup>fl/fl</sup>* [B6.129P2(129S4)-*Ago2<sup>tm1.1Tara</sup>/J*, 016520] (33), *Kras<sup>LSL-G12D</sup>* (B6.129S4-*kras*<sup>tm4Tyji</sup>/J, 08179) (46), *p53<sup>fl/fl</sup>* [B6.129P2-*Trp53<sup>tm1Brnj</sup>*/J, 008462] (52), and *CCSP-Cre* [B6N.129S6(Cg)-*Scgb1a1<sup>tm1(CreERT)Blh</sup>*/J] (34). Jackson breeds each on a C57BL/6J background. At our institution, animals were maintained in pathogen-free housing with a 12-h light/dark cycle and ad libitum access to food and water. Equal numbers of male and female mice were used for all experiments. The University of Michigan Institutional Animal Care and Use Committee approved all animal work.

**Intratracheal Adenovirus Administration.** Cre-expressing adenovirus (Adeno-Cre) was obtained from the Viral Vector Core Facility at the University of Iowa. The virus was delivered by intratracheal administration as described (31). Briefly, mice aged 6 to 8 wk were anesthetized with isoflurane and then infected with

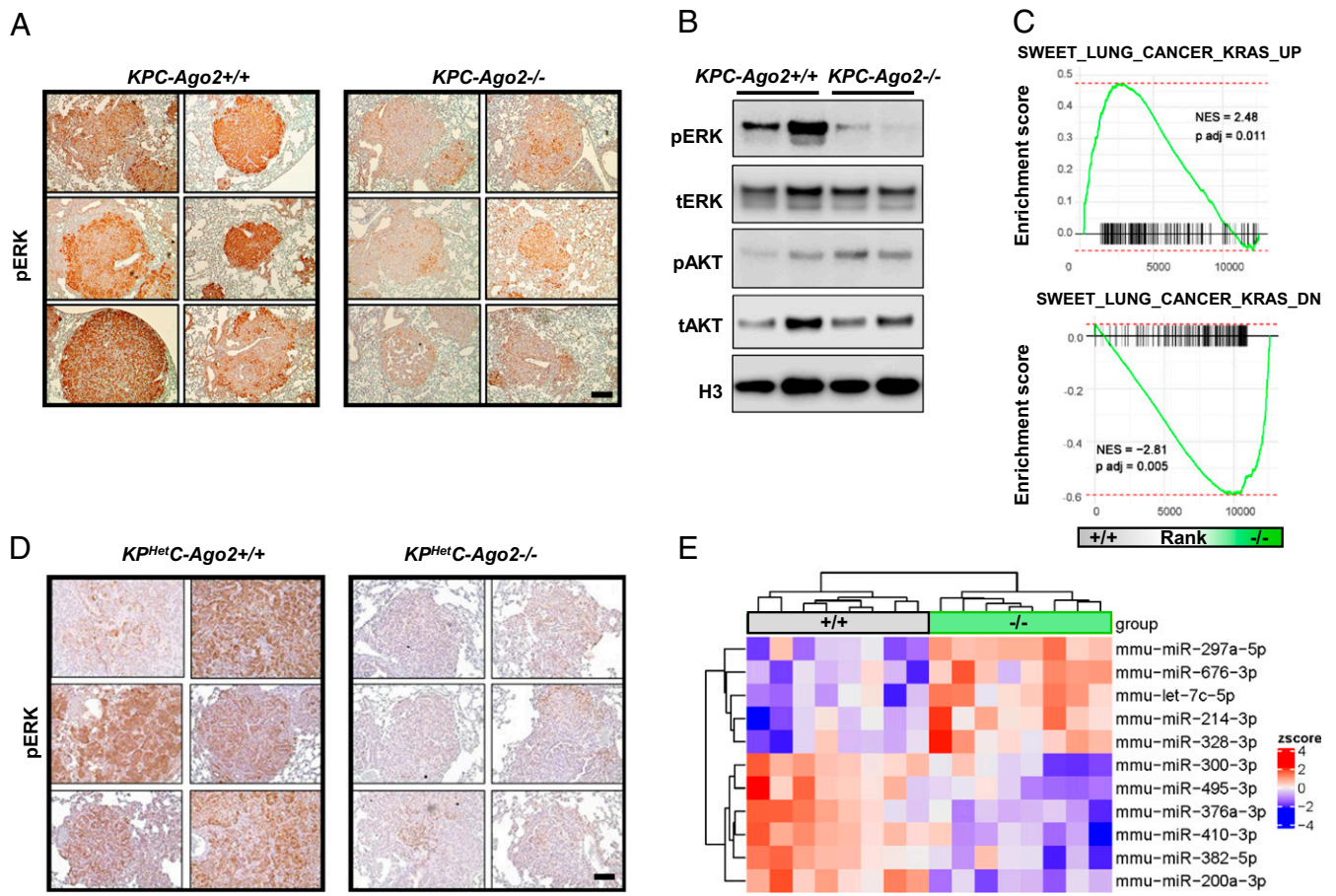


**Fig. 4.** *Ago2* ablation reduces *Kras* signaling in vivo. (A) pERK immunohistochemistry of lung cross-sections from *KPC-Ago2*<sup>+/+</sup> versus *KPC-Ago2*<sup>-/-</sup> mice. (Scale bar, 50  $\mu$ m.) (B) Immunoblot analysis of protein lysates from isolated lung nodules of *KPC-Ago2*<sup>+/+</sup> and *KPC-Ago2*<sup>-/-</sup> mice. Phosphorylated ERK (pERK), total ERK (tERK), phosphorylated AKT (Ser-473) (pAKT), total AKT (tAKT), and histone H3 (H3). (C) GSEA assessing genes associated with increased KRAS signaling (SWEET\_LUNG\_CANCER\_KRAS\_UP and SWEET\_LUNG\_CANCER\_KRAS\_DOWN). Comparison of genes differentially expressed in *KPC-Ago2*<sup>+/+</sup> versus *KPC-Ago2*<sup>-/-</sup> (isolated nodules). NES, normalized enrichment score. (D) pERK immunohistochemistry of lung cross-sections from *KP*<sup>HetC</sup>-*Ago2*<sup>+/+</sup> and *KP*<sup>HetC</sup>-*Ago2*<sup>-/-</sup> mice. (Scale bar, 100  $\mu$ m.) (E) Heat map of differentially expressed (false discovery rate [FDR] < 0.05) species from miRNA QPCR performed on nodules from *KPC* mice with normal *Ago2* (<sup>+/+</sup>) or with biallelic *Ago2* knockout (<sup>-/-</sup>).

1.25  $\times 10^7$  plaque-forming units (PFUs) of Adeno-Cre in 67.5  $\mu$ L vehicle through a micropipette tip inserted into the pharynx. After mice regained consciousness, the same procedure was repeated, such that each mouse received a total of 2.5  $\times 10^7$  PFUs in 125  $\mu$ L vehicle. Viral administration was performed in a biosafety level 2+ room, in accordance with the guidelines of the University of Michigan Institutional Biosafety Committee.

**Tamoxifen Administration.** Tamoxifen (Sigma) was dissolved in corn oil to a concentration of 20 mg/mL and administered to 6-wk-old mice by intraperitoneal injection at a dose of 0.25 mg/kg body weight once every other day for four doses.

**Tissue Collection and Immunohistochemistry.** At time points indicated for tissue harvest, mice were killed by isoflurane overdose. Lungs were inflated with phosphate-buffered saline (PBS) administered through the trachea. Left, superior, and postcaval lobes were isolated, fixed overnight in formalin at 4  $^{\circ}$ C, then transferred to 70% ethanol. After processing and paraffin embedding, tissue sections were cut to a thickness of 5  $\mu$ m. Hematoxylin and eosin (H&E) staining was performed according to standard protocol. For immunohistochemical (IHC) staining, slides were deparaffinized and treated with Antigen Unmasking Solution (Vector Laboratories, H-3300); then, endogenous peroxidases were inactivated by incubation in 3% hydrogen peroxide (Sigma). Primary antibodies used (with dilutions) are as follows: AGO2 (Sino Biologicals, 50683-RO-36) 1:100; Ki67 (BD Biosciences, 550609) 1:500; Phospho-Erk1/2 (Cell Signaling, 4376S) 1:100; and Phospho-Akt (Cell Signaling, 4060S) 1:100 were diluted in 10% normal goat serum (NGS) (in PBS). Antibody detection was achieved with species-specific VECTSTAIN Elite

ABC kits (Vector Labs) and a DAB Peroxidase Substrate kit (Vector Labs). All slides were analyzed by a board-certified pathologist.

**Mouse Lung Nodule Isolation and Ex Vivo Culture.** Lung dissociation and organoid culture were performed as previously described (41, 42) with scissors. Samples were then digested for 1 h at 37  $^{\circ}$ C in a mixture of dispase (1 mg/mL) (BD Biosciences), trypsin/2 mM ethylenediaminetetraacetic acid (EDTA) (0.25% by volume) (Cellgro), and elastase (10 U/mL) (Worthington). Dissociated cells were passed through a 70- $\mu$ m cell strainer and resuspended in organoid culture medium (OCM) containing the following: Dulbecco's Modified Eagle Medium (DMEM)/F12 supplemented with 1xITS (insulin, transferrin, and selenium; Invitrogen), 0.5% BPE (bovine pituitary extract; Fisher), 25 ng/mL mEGF (epidermal growth factor; PeproTech), 0.1  $\mu$ g/mL CTX (cholera toxin; Sigma), 10  $\mu$ M Y-27632 (ROCK inhibitor; Sigma), 100 nM retinoic acid (Cayman), and 100 units/mL penicillin-streptomycin (Gibco, Cat. No. 10378016). Aliquots of 1  $\times 10^4$  cells, in 50  $\mu$ L OCM, were mixed with 50  $\mu$ L Growth Factor Reduced Matrigel (Corning) and plated into the center of single wells in Poly-D-Lysine Cellware 12-well plates (Corning). After 30 min in a 37  $^{\circ}$ C cell culture incubator supplemented with 5% CO<sub>2</sub>, OCM was added to each well and changed every 2 d for the duration of the experiment. Two-dimensional culture of organoid cells for in vitro transfection experiments was performed as follows: Trypsinized organoid pellets were transferred to six-well collagen-coated plates (Corning) containing OCM. Cells were allowed to adhere overnight after which they were transfected with indicated AGO2 constructs (12, 13) using Lipofectamine 3000 (Thermo Fisher Scientific). Proliferation of cultured cells was analyzed using the



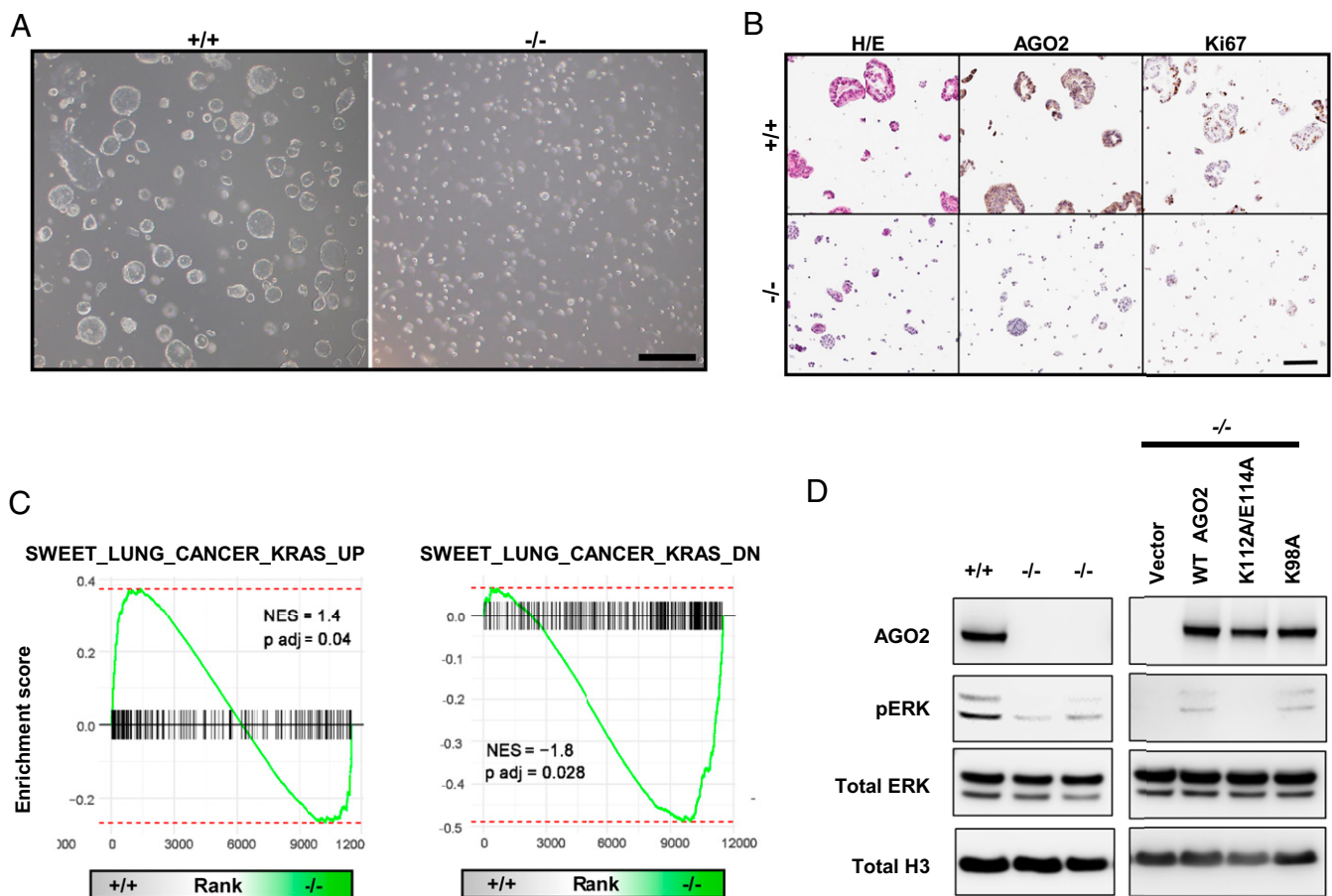


**Fig. 5.** AGO2 promotes MAPK signaling through direct interaction. (A) Organoids isolated from lung nodules of *KPC-Ago2*<sup>+/+</sup> versus *KPC-Ago2*<sup>-/-</sup> mice. Bright field image. (Scale bar, 500  $\mu$ m.) (B) Histological sections of *KPC-Ago2*<sup>+/+</sup> and *KPC-Ago2*<sup>-/-</sup> organoids stained with H&E and antibodies directed against AGO2 and Ki67. (Scale bar, 150  $\mu$ m.) (C) GSEA assessing genes associated with increased KRAS signaling (SWEET\_LUNG\_CANCER\_KRAS\_UP and SWEET\_LUNG\_CANCER\_KRAS\_DN). Comparison of genes differentially expressed in *KPC-Ago2*<sup>+/+</sup> versus *KPC-Ago2*<sup>-/-</sup> organoids. NES, normalized enrichment score. (D, Left) Immunoblot analysis of protein lysates from *KPC-Ago2*<sup>+/+</sup> versus *KPC-Ago2*<sup>-/-</sup> organoid-derived cells. Phosphorylated ERK (pERK), total ERK (tERK), and histone H3 (H3). (D, Right) Immunoblot analysis of *KPC-Ago2*<sup>-/-</sup> organoid-derived cells transfected with constructs encoding wild-type AGO2 (WT AGO2), AGO2K112A/E114A (K112A/E114A), and AGO2K98A (K98A).

Incucyte live cell imaging system (Sartorius). Lysis and immunoblotting (described below) were performed 72 h after transfection.

**Immunoblotting and Immunoprecipitation.** Cells were lysed in ice-cold radioimmunoprecipitation assay (RIPA) buffer (Pierce) supplemented with phosphatase inhibitor mixture. Protein concentration was quantified using the Bio-Rad Protein Assay. Between 10 and 30  $\mu$ g of total protein was separated on 4–12% Bis-Tri gradient gels (Life Technologies) by sodium dodecyl sulfate polyacrylamide gel electrophoresis (SDS-PAGE) and then transferred to nitrocellulose membranes. Antibodies are indicated as follows: Ago2 (Sino Biologicals, 50683-RO-36) 1:1,000; GAPDH(14C10) (Cell Signaling, 36835) 1:1,000; H3 (Cell Signaling, 9715) 1:1,000; Phospho-Erk1/2 (Cell Signaling, 4376S) 1:1,000; Erk1/2 (Cell Signaling, 9102S) 1:1,000; Phospho-Akt (Cell Signaling, 4060S) 1:1,000; and Akt (Cell Signaling, 2920S) 1:1,000. Immunoprecipitation experiments were carried out using 300  $\mu$ g cell lysate. This was precleared with Protein A/G agarose beads for 1 h at 4  $^{\circ}$ C. Following incubation, lysates were treated with 5  $\mu$ g of Ras antibody (Ras10 monoclonal antibody, Millipore) or 5  $\mu$ g IgG isotype control overnight at 4  $^{\circ}$ C. Subsequently, Protein A/G agarose beads were used to precipitate immune complexes (2-h incubation at 4  $^{\circ}$ C). Immunoprecipitates were then washed, resuspended in loading buffer, and analyzed by immunoblot.

**Transcriptome Analysis.** mRNA isolated as indicated above was quantitated on the Illumina platform using RiboErase methodology. Transcripts were quantified by pseudoalignment algorithm Kallisto (53) with mm10 as the reference genome. Estimated counts were used to create DEGLIST and normalized by trimmed mean of M values (TMM) (54) using the calcNormFactors

of edgeR (55). Lowly expressed genes with mean transcript per million (TPM) of less than 1 were removed from downstream analysis. Differential analysis between biallelic knockout and wild type was performed on voom-transformed count data (56) using the limma (57) package. Finally, the fgsea package was used to perform gene set analysis using estimated log-fold change from differential analysis as input. Mouse genes were converted to human homologs using biomaRT (58) before evaluating enrichment of gene sets. Enrichment plots and heat maps were generated in R Studio.

**MicroRNA Expression Profiles Using Quantitative PCR of Mouse miRNome Panels.** Total RNA was isolated from lung nodules using the AllPrep DNA/RNA/miRNA Universal Kit (Qiagen). Five nanograms of RNA from each sample was converted into cDNA using the miRCURY LNA Universal RT microRNA PCR Universal cDNA Synthesis Kit II. Quantitative micro RT-PCR was performed using exiLent SYBR Green master mix with microRNA ready-to-use PCR mix, Mouse&Rat panel I, V4.M (Exiqon) on an ABI 7900HT Fast Real Time PCR system (Applied Biosystems). Data were analyzed using GenEX version 6 software.

**Statistical Analysis.** Intergroup comparisons were made with Student's *t* test (two-group comparisons) or one-way ANOVA (three-group comparisons). For RNA-seq, a moderated *t* test implemented with limma was used for group comparison and *P* value adjustment for multitest was made with the Benjamini-Hochberg (BH) method. For microRNA, significance was tested with a Wilcoxon signed-rank test. Statistical significance was defined as a *P* value <0.05 (BH adjusted *P* value for RNA-seq).

**Data Availability.** All study data are included in the article and/or *SI Appendix*.

**ACKNOWLEDGMENTS.** This work was supported by the Prostate Cancer Foundation, Prostate SPORE Grant P50 CA186786, National Cancer Institute

Outstanding Investigator Award R35 CA231996, and the Early Detection Research Network U01 NIH Grant CA214170. A.M.C. is a Howard Hughes Medical Institute Investigator, an A. Alfred Taubman Scholar, and an American Cancer Society Professor.

1. R. L. Siegel, K. D. Miller, A. Jemal, Cancer statistics, 2017. *CA Cancer J. Clin.* **67**, 7–30 (2017).
2. D. S. Ettinger *et al.*; NCCN (National Comprehensive Cancer Network), Non-small cell lung cancer. *J. Natl. Compr. Canc. Netw.* **10**, 1236–1271 (2012).
3. S. Schubbert, K. Shannon, G. Bollag, Hyperactive Ras in developmental disorders and cancer. *Nat. Rev. Cancer* **7**, 295–308 (2007).
4. A. E. Karnoub, R. A. Weinberg, Ras oncogenes: Split personalities. *Nat. Rev. Mol. Cell Biol.* **9**, 517–531 (2008).
5. M. Trahey, F. McCormick, A cytoplasmic protein stimulates normal N-ras p21 GTPase, but does not affect oncogenic mutants. *Science* **238**, 542–545 (1987).
6. R. J. Shaw, L. C. Cantley, Ras, PI(3)K and mTOR signalling controls tumour cell growth. *Nature* **441**, 424–430 (2006).
7. P. Garrido *et al.*, Treating KRAS-mutant NSCLC: Latest evidence and clinical consequences. *Ther. Adv. Med. Oncol.* **9**, 589–597 (2017).
8. A. D. Cox, S. W. Fesik, A. C. Kimmelman, J. Luo, C. J. Der, Drugging the undruggable RAS: Mission possible? *Nat. Rev. Drug Discov.* **13**, 828–851 (2014).
9. C. R. Lindsay, M. Jamal-Hanjani, M. Forster, F. Blackhall, KRAS: Reasons for optimism in lung cancer. *Eur. J. Cancer* **99**, 20–27 (2018).
10. M. R. Janes *et al.*, Targeting KRAS mutant cancers with a covalent G12C-specific inhibitor. *Cell* **172**, 578–589.e17 (2018).
11. D. S. Hong *et al.*, KRAS<sup>G12C</sup> inhibition with sotorasib in advanced solid tumors. *N. Engl. J. Med.* **383**, 1207–1217 (2020).
12. S. Shankar *et al.*, KRAS engages AGO2 to enhance cellular transformation. *Cell Rep.* **14**, 1448–1461 (2016).
13. S. Shankar *et al.*, An essential role for Argonaute 2 in EGFR-KRAS signaling in pancreatic cancer development. *Nat. Commun.* **11**, 2817 (2020).
14. T. Sasaki, A. Shiohama, S. Minoshima, N. Shimizu, Identification of eight members of the Argonaute family in the human genome. *Genomics* **82**, 323–330 (2003).
15. P. N. Valdmans *et al.*, Expression determinants of mammalian Argonaute proteins in mediating gene silencing. *Nucleic Acids Res.* **40**, 3704–3713 (2012).
16. G. Hutvagner, P. D. Zamore, A microRNA in a multiple-turnover RNAi enzyme complex. *Science* **297**, 2056–2060 (2002).
17. G. Hutvagner, M. J. Simard, Argonaute proteins: Key players in RNA silencing. *Nat. Rev. Mol. Cell Biol.* **9**, 22–32 (2008).
18. G. Meister *et al.*, Human Argonaute2 mediates RNA cleavage targeted by miRNAs and siRNAs. *Mol. Cell* **15**, 185–197 (2004).
19. S. Cheloufi, C. O. Dos Santos, M. M. Chong, G. J. Hannon, A dicer-independent miRNA biogenesis pathway that requires Ago catalysis. *Nature* **465**, 584–589 (2010).
20. A. Frohn *et al.*, Dicer-dependent and -independent Argonaute2 protein interaction networks in mammalian cells. *Mol. Cell. Proteomics* **11**, 1442–1456 (2012).
21. J. Winter, S. Diederichs, Argonaute proteins regulate microRNA stability: Increased microRNA abundance by Argonaute proteins is due to microRNA stabilization. *RNA Biol.* **8**, 1149–1157 (2011).
22. J. Lu *et al.*, MicroRNA expression profiles classify human cancers. *Nature* **435**, 834–838 (2005).
23. J. Takamizawa *et al.*, Reduced expression of the let-7 microRNAs in human lung cancers in association with shortened postoperative survival. *Cancer Res.* **64**, 3753–3756 (2004).
24. E. Chirshv, K. C. Oberg, Y. J. Ioffe, J. J. Unteraehrer, Let-7 as biomarker, prognostic indicator, and therapy for precision medicine in cancer. *Clin. Transl. Med.* **8**, 24 (2019).
25. L. Li, C. Yu, H. Gao, Y. Li, Argonaute proteins: Potential biomarkers for human colon cancer. *BMC Cancer* **10**, 38 (2010).
26. N. Cheng, Y. Li, Z. G. Han, Argonaute2 promotes tumor metastasis by way of up-regulating focal adhesion kinase expression in hepatocellular carcinoma. *Hepatology* **57**, 1906–1918 (2013).
27. O. Vaksman, T. E. Hetland, C. G. Trope, R. Reich, B. Davidson, Argonaute, Dicer, and Drosha are up-regulated along tumor progression in serous ovarian carcinoma. *Hum. Pathol.* **43**, 2062–2069 (2012).
28. J. Shen *et al.*, EGFR modulates microRNA maturation in response to hypoxia through phosphorylation of AGO2. *Nature* **497**, 383–387 (2013).
29. J. Zhang *et al.*, Up-regulation of Ago2 expression in gastric carcinoma. *Med. Oncol.* **30**, 628 (2013).
30. E. Cerami *et al.*, The cBio cancer genomics portal: An open platform for exploring multidimensional cancer genomics data. *Cancer Discov.* **2**, 401–404 (2012).
31. M. DuPage, A. L. Dooley, T. Jacks, Conditional mouse lung cancer models using adenoviral or lentiviral delivery of Cre recombinase. *Nat. Protoc.* **4**, 1064–1072 (2009).
32. C. Sheridan, J. Downward, Overview of KRAS-driven genetically engineered mouse models of non-small cell lung cancer. *Curr. Protoc. Pharmacol.* **70**, 14 35 1–14 35 16 (2015).
33. D. O’Carroll *et al.*, A Slicer-independent role for Argonaute 2 in hematopoiesis and the microRNA pathway. *Genes Dev.* **21**, 1999–2004 (2007).
34. E. L. Rawlins *et al.*, The role of Scgb1a1+ Clara cells in the long-term maintenance and repair of lung airway, but not alveolar, epithelium. *Cell Stem Cell* **4**, 525–534 (2009).
35. H. Ji *et al.*, K-ras activation generates an inflammatory response in lung tumors. *Oncogene* **25**, 2105–2112 (2006).
36. X. Xu *et al.*, The cell of origin and subtype of K-Ras-induced lung tumors are modified by Notch and Sox2. *Genes Dev.* **28**, 1929–1939 (2014).
37. A. Sweet-Cordero *et al.*, An oncogenic KRAS2 expression signature identified by cross-species gene-expression analysis. *Nat. Genet.* **37**, 48–55 (2005).
38. X. Chen, J. Du, R. Jiang, L. Li, MicroRNA-214 inhibits the proliferation and invasion of lung carcinoma cells by targeting JAK1. *Am. J. Transl. Res.* **10**, 1164–1171 (2018).
39. X. Zhao *et al.*, MicroRNA-214 governs lung cancer growth and metastasis by targeting carboxypeptidase-D. *DNA Cell Biol.* **35**, 715–721 (2016).
40. Y. Li, L. Zhao, Y. Qi, X. Yang, MicroRNA-214 upregulates HIF-1 $\alpha$  and VEGF by targeting ING4 in lung cancer cells. *Mol. Med. Rep.* **19**, 4935–4945 (2019).
41. C. E. Barkauskas *et al.*, Type 2 alveolar cells are stem cells in adult lung. *J. Clin. Invest.* **123**, 3025–3036 (2013).
42. T. Peng *et al.*, Hedgehog actively maintains adult lung quiescence and regulates repair and regeneration. *Nature* **526**, 578–582 (2015).
43. S. Dearden, J. Stevens, Y. L. Wu, D. Blowers, Mutation incidence and coincidence in non small-cell lung cancer: meta-analyses by ethnicity and histology (mutMap). *Ann. Oncol.* **24**, 2371–2376 (2013).
44. I. Z. Uras, H. P. Moll, E. Casanova, Targeting KRAS mutant non-small-cell lung cancer: Past, present and future. *Int. J. Mol. Sci.* **21**, 4325 (2020).
45. F. Skoulidis *et al.*, Co-occurring genomic alterations define major subsets of KRAS-mutant lung adenocarcinoma with distinct biology, immune profiles, and therapeutic vulnerabilities. *Cancer Discov.* **5**, 860–877 (2015).
46. E. L. Jackson *et al.*, Analysis of lung tumor initiation and progression using conditional expression of oncogenic K-ras. *Genes Dev.* **15**, 3243–3248 (2001).
47. R. B. Blasco *et al.*, c-Raf, but not B-Raf, is essential for development of K-Ras oncogene-driven non-small cell lung carcinoma. *Cancer Cell* **19**, 652–663 (2011).
48. J. A. Engelman *et al.*, Effective use of PI3K and MEK inhibitors to treat mutant Kras G12D and PIK3CA H1047R murine lung cancers. *Nat. Med.* **14**, 1351–1356 (2008).
49. C. L. Trejo, J. Juan, S. Vicent, A. Sweet-Cordero, M. McMahon, MEK1/2 inhibition elicits regression of autochthonous lung tumors induced by KRASG12D or BRAFV600E. *Cancer Res.* **72**, 3048–3059 (2012).
50. P. A. Jänne *et al.*, Selumetinib plus docetaxel for KRAS-mutant advanced non-small-cell lung cancer: A randomised, multicentre, placebo-controlled, phase 2 study. *Lancet Oncol.* **14**, 38–47 (2013).
51. M. Cicchini *et al.*, Context-dependent effects of amplified MAPK signaling during lung adenocarcinoma initiation and progression. *Cell Rep.* **18**, 1958–1969 (2017).
52. S. Marino, M. Vooijs, H. van Der Gulden, J. Jonkers, A. Berns, Induction of medulloblastomas in p53-null mutant mice by somatic inactivation of Rb in the external granular layer cells of the cerebellum. *Genes Dev.* **14**, 994–1004 (2000).
53. N. L. Bray, H. Pimentel, P. Melsted, L. Pachter, Near-optimal probabilistic RNA-seq quantification. *Nat. Biotechnol.* **34**, 525–527 (2016).
54. M. D. Robinson, A. Oshlack, A scaling normalization method for differential expression analysis of RNA-seq data. *Genome Biol.* **11**, R25 (2010).
55. M. D. Robinson, D. J. McCarthy, G. K. Smyth, edgeR: A Bioconductor package for differential expression analysis of digital gene expression data. *Bioinformatics* **26**, 139–140 (2010).
56. C. W. Law, Y. Chen, W. Shi, G. K. Smyth, voom: Precision weights unlock linear model analysis tools for RNA-seq read counts. *Genome Biol.* **15**, R29 (2014).
57. M. E. Ritchie *et al.*, Limma powers differential expression analyses for RNA-sequencing and microarray studies. *Nucleic Acids Res.* **43**, e47 (2015).
58. S. Durinck, P. T. Spellman, E. Birney, W. Huber, Mapping identifiers for the integration of genomic datasets with the R/Bioconductor package biomaRt. *Nat. Protoc.* **4**, 1184–1191 (2009).